Nanoscale
Advances

ROYAL SOCIETY
OF CHEMISTRY

PAPER

View Article Online
View Journal

Check for updates

Cite this: DOI: 10.1039/d5na00976f

Impact of static and dynamic magneto-mechanical stimulation with vortex microdiscs on glioblastoma cells cultured on 2D substrates with physiological stiffness

Andrea Visonà, *[ab] Sébastien Soulan,[a] Bernard Dieny, [b] Robert Morel [b] and Alice Nicolas [a]

Received 16th October 2025
Accepted 22nd April 2026

DOI: 10.1039/d5na00976f

rsc.li/nanoscale-advances

External mechanical stresses acting on cellular compartments critically regulate cell behaviour and can induce cell death. Magnetically actuated particles present a promising strategy to apply such forces in a controlled manner, with potential applications in cancer therapy. In this study, we investigate the effects of actuating vortex magnetic microdiscs on a glioblastoma cell line cultured on soft, biomimetic substrates that mimic *in vivo* stiffness. Using a Halbach array, we applied either static mechanical compression or a combination of compressive and low-frequency vibrational stresses (2–20 Hz). Our results demonstrate that both compressive and vibrational stresses impair important cellular functions associated with glioblastoma persistence in a dose-dependent and stiffness-dependent manner. In particular, on soft 2D substrates, sufficiently strong compressive loads limit proliferation, while the addition of vibrations alters cell motility, cell morphology and the actomyosin machinery. Our findings demonstrate that magnetic particle-mediated mechanical stimulation can disrupt glioblastoma cell aggressiveness in physiologically relevant 2D substrates, supporting its potential as an adjunct to conventional chemo- and radiotherapies by both inducing cell death and limiting resistant populations.

1 Introduction

The application of mechanical stresses to cellular compartments is known to influence cellular functions and can even cause cell death.[1–3] In this context, applying intracellular mechanical stresses is being considered as a potential adjunctive treatment for some pathologies. For instance, nuclear compression triggers a change in cell migration mode,[4] and the deformation of the membranes of the Golgi apparatus or of the endoplasmic reticulum affects the flow of calcium or other ions, with consequences for cell metabolism, polarity, migration, and proliferation.[1] These forces may arise from the stimulation of internal agents, such as actin fibre contraction or osmotic imbalance.[5] They may also be caused by external stresses such as hydrodynamic flows. Recently, advanced microsystems based on optical or magnetic traps have been developed to remotely apply controlled mechanical stresses to precise locations in cells.[6–8] For example, magnetic particles have been used to apply traction forces on neurites and improve their outgrowth in the context of neural regeneration.[9,10] Similar particles were set in vibration using an alternating magnetic field to stimulate insulin secretion in pancreatic cells[11] or calcium influx in mechanosensory neurons.[12] Several studies have also shown that magnetic particles set in vibration in the Hz range could induce cancer cell death,[13–18] possibly by mechanically altering the plasma or lysosome membranes.

More specifically, the use of magnetically actuated particles has opened perspectives for the cure of glioblastoma, a lethal cancer for which no curative treatment is currently available.[19] The challenge in curing glioblastoma arises in four main factors: its invasiveness (aggressive migration behaviour), heterogeneity (both inter-patient and intra-tumour), its rapid development and its resistance to chemotherapy.[20] In addition, there is the difficulty of circumnavigating the brain–blood barrier that, while protecting the brain and making it a highly controlled and exclusive environment, represents a real challenge for molecules to be effectively delivered to brain tumours. In a pioneering study, Kim *et al.*[13] showed that low frequency vibrations of magnetic microdiscs attached to the cell membrane could trigger apoptotic pathways in relation to the stretching of the plasma membrane and the activation of specific ion channels. Since then, several groups have shown that internalised particles set into vibration at a frequency of a few tens of Hz could efficiently kill model glioblastoma cells.[15–17] In contrast to radiotherapy, the first-line treatment for glioblastoma, particle-based treatment may target specific cell

---

[a] Univ. Grenoble Alpes, CNRS, CEA/LETI-Minatec, Grenoble INP, LTM, Grenoble F-38000, France. E-mail: andrea.visona96@gmail.com

[b] Univ. Grenoble Alpes, CEA, CNRS, Spintec, Grenoble F-38000, France

populations by biofunctionalising the surface of the particles. However, it has been shown that killing cancer cells was not successful in eradicating glioblastoma, as the surviving cells drift toward more aggressive phenotypes.[21] For this reason, a combination of treatments that both destroy cancer cells and limit the aggressiveness of the surviving ones is currently underway.[22] Regarding magnetic particles, once the mechanical forces they transmit have been optimised, they could be used as adjunctive treatment, enhancing the efficacy of primary therapy and limiting the activity of cells resistant, for example, to radiotherapy.[23]

In previous studies, the *in vitro* demonstrations of the efficacy of treating cells with vibrating particles were carried out in standard culture plates, with plastic surfaces (see ref. 24,25 for a review). However, the effectiveness of the vibrating particles to kill cancer cells was reduced in cells grown in spheroids[25] or *in vivo*.[15,26] A basic limitation of standard plastic plates is that, while they are highly effective in enabling cell growth and imaging, these culture conditions put cells in a mechanical environment bearing little or no resemblance to that encountered *in vivo*, for instance being a million times stiffer.[27,28] This is of primary importance, since the mechanical properties of the extracellular environment have been shown to be a key determinant of invasion, proliferation, and resistance to radiochemotherapy in glioblastoma.[29–31] Although the difference between the *in vitro* and the *in vivo* assays cannot be solely attributable to the difference in mechanical properties of the extracellular environment, the interaction of the magnetic particles with cells, as well as the signalling pathways involved in cellular functions such as proliferation or migration, are regulated differently under these culture conditions.[32–34] Standard culture conditions are for instance known to induce drifts of cell phenotypes,[35] while cells grown either on soft substrates mimicking the stiffness of the tissue of interest or in 3D as spheroids were shown to better preserve cellular phenotypes.[36,37]

In this context, we questioned whether mild stresses applied by internalised particles could impair some basic cellular functions involved in glioblastoma aggressiveness, for instance cell migration and proliferation, when the cells display a physiologically relevant level of contractility. To this end, a model glioblastoma cell line was grown *in vitro* on soft supports whose stiffness matches that of glioblastoma tissues to achieve a relevant mimicry of the cellular characteristics encountered *in vivo*. These simple substrates provide an easy platform to optimise the intracellular forces generated by the particles, before moving to more advanced *in vitro* systems. Following previous studies from our group and others, we used magnetically actuated vortex microdiscs (MDs) to apply mechanical stresses.[24] Vortex microdiscs are highly anisotropic particles in which the magnetisation in the absence of a field has a vortex configuration. This configuration limits the remanent magnetisation of the particles and enables them to remain dispersed. Alternating or rotating magnetic fields with a frequency of a few Hz or tens of Hz were shown to set the MDs in vibration or rotation. This treatment was shown to trigger cell death *in vitro* in a dose-dependent manner. In addition, it was shown that increasing the frequency had a decreasing impact on cell viability, suggesting that vibrations in the Hz regime may have a stronger impact on cell fate compared to tens of Hz.[13] This raises the question of whether a static magnetic stimulation of the MDs, resulting in a static mechanical force, may also alter cell functioning. In this context, we analysed the impact of intracellular mechanical stimulations consisting of either a static mechanical stress or the superimposition of static and dynamic vibrational stresses in the range of 2 to 20 Hz, all mediated by the MDs.

In this article, we thus report on the sensitivity of U87-MG cells to compressive and vibrating stresses resulting from the actuation of magnetic microdisc cells, highlighting a dose-dependent effect and sensitivity to the elastic properties of the extracellular environment, the more pronounced impact being observed in cells grown on soft, biomimetic substrates. We show that gentle mechanical stimulation, obtained with a minimal dose of particles, impairs cell proliferation and motility, while irreversible alteration of the cell shape is observed with particles vibrating between 10 and 20 Hz. Furthermore, we observe that sufficiently large static compressive forces can impair cell proliferation, although vibrating mechanical stresses have a more pronounced effect, with increased persistence at higher frequency. The impairment of cell proliferation and motility is attributed to alterations of cell vimentin and actin cytoskeletons that are shown to drive changes in cell contractile capabilities. By demonstrating that intracellular mechanical stimulation, combining compression and vibration, can both induce cell death and alteration of fundamental cellular functions such as cell contractility, our results suggest a mechanistic link between externally applied forces and the activation of mechanotransduction pathways involved in more complex biological processes such as proliferation and migration. A precise identification of the molecular actors underlying this response, such as specific ion channels or associated signaling axes, remains to be established. Elucidating these pathways will be essential to define the direct targets of particle-mediated mechanical stimulation and to optimise its potential use as an adjuvant strategy in cancer therapy alongside chemotherapy or radiotherapy.

2 Methods

2.1 Magnetic microdisc fabrication and characterisation

The vortex micro-discs were fabricated using a top-down approach as previously described.[38] Briefly, a double layer of PMMA positive resist and ma-N negative resist was deposited onto a 100 mm silicon wafer and patterned using deep ultraviolet optical lithography to create an array of circular wells with a diameter of 1.3 μm in the ma-N resist. After developing the ma-N resist, three successive metal layers – gold (10 nm), permalloy ($Ni_{80}Fe_{20}$, 60 nm), and gold (10 nm) – were deposited using electron-beam evaporation (Fig. 1a). A first ethanol lift-off allowed removing the top ma-N resist, leaving the array of particles attached to the base PMMA resist (Fig. 1b). The magnetic properties of the particles were characterised using vibrating sample magnetometry (MicroSense EasyVSM). Fig. 1c

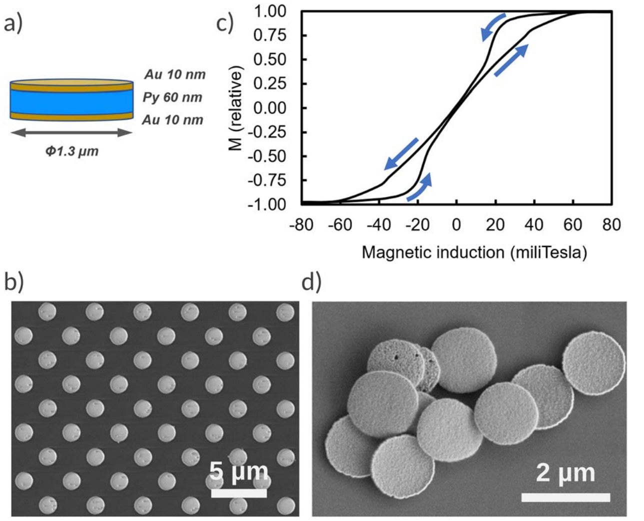

Fig. 1 (a) Schematics of the structure of vortex microdiscs. (b) Microdisc array still attached to the PMMA resist, after lift-off of the ma-N resist. (c) Normalised hysteresis loop of the microdiscs attached to the silicon wafer with an in-plane magnetic field (scan directions of the field are shown by the arrows). (d) Liberated microdiscs, after lift-off of the PMMA resist.

shows the magnetisation curve with an in-plane applied magnetic field, indicating a 60 mT saturation field and a very low magnetic remanence. As already reported, the low remanence ensures that the particles do not aggregate when they are released in a liquid.[38] On the other hand, due to their low saturation field, the particles can be remotely actuated using permanent magnet devices. A second acetone lift-off allowed the particles to be detached from the PMMA base resist (Fig. 1d). Particles were sonicated three times with hot acetone to remove any resist monomer, after which they were washed three more times with ethanol and stored in ethanol. The geometric and structural specifications of the free vortex particles were obtained by SEM imaging as described in ref. 32. Prior to use, particles were dispersed by sonication and the ethanol was replaced with culture medium, with extensive rinsing steps to minimise cell exposure to ethanol.

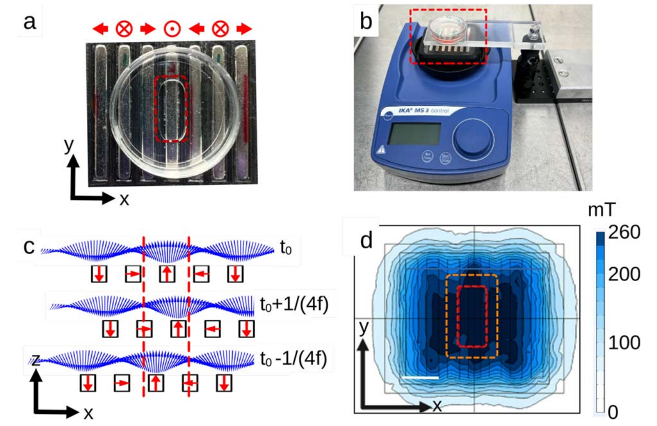

Fig. 2 (a) Top view picture of the rare-earth magnets array in a planar Halbach configuration, with a 35 mm diameter Petri dish. The red dashed rectangle indicates the zone of the dish used for cell culture. The schematic at the top shows the magnets' magnetisation direction. (b) The orbital stirrer with the magnet array and the suspended Petri dish. The magnitude of the magnetic field is adjusted through the distance between the Petri dish and the magnet array. (c) Side view of the magnetic induction field **B** (blue arrows) 4 mm above the array centre when the stirrer undergoes orbital motion. Field components B_x and B_z vary sinusoidally while the magnitude (arrow length) remains constant. Red arrows show the magnetisation of the individual magnets in the array. Red dashed lines mark the cell culture region (the same as (a)). In this region, the array's orbital motion in the *xy* plane produces an oscillating field, shown here in the *xz* plane. Panels depict the static condition (t_0) and the maximal magnet displacements along *x* at $t_0 \pm 1/(4f)$, where f is the oscillation frequency. (d) Magnitude of the oscillating field (bar 1 cm). Red dashed lines mark the region where cells are exposed to the static field; the orange rectangle shows the expanded exposure area when the magnet array undergoes orbital motion. With the Petri dish positioned 4 mm above the magnets and cells arranged as in (a), they experience an oscillating magnetic field with an amplitude of 250 mT, an angular excursion of 55°, and frequencies up to 25 Hz.

2.2 Magnetic field device

The magnetic field was generated by an array of seven rare-earth magnets (NdFeB N42 magnets, Supermagnete, Gottmadingen, Germany) assembled in a planar Halbach configuration.[39] The array is attached to an orbital stirrer (IKA MS3 Digital, Staufen, Germany) and set into motion under a fixed cell culture plate (Fig. 2a and b). The size of the magnets is $40\times 8 \times 4$ mm^3, with the magnetisation either parallel to the horizontal x axis or the vertical z axis according to the position in the Halbach array. The spacing between magnets is 3 mm. The width and spacing of the magnets are optimised such that, over the center region of the array: (1) the field amplitude is almost constant at a distance of 4 mm above the magnets and (2) given the orbital amplitude of the stirrer rotation (4.5 mm), the angular variation in the field direction at a fixed point above the array is maximum (Fig. 2c and d). Under these conditions, the field components B_x and B_z vary sinusoidally, while the magnitude remains essentially constant. When the magnet array moves beneath the cells, its orbital motion in the xy plane produces an oscillatory translation of the field along x, as illustrated in Fig. 2c at successive time points. Overall, the device allows for an oscillating magnetic field of 250 mT, with an angular amplitude of 55° and a frequency up to 25 Hz. This relatively high field compared to the literature[25] was selected to ensure saturation of the MDs irrespective of their orientation within the cell. As shown in Fig. 2c, the applied field is primarily out-of-plane, requiring a larger amplitude to saturate the particles compared to the in-plane configuration shown in Fig. 1c. The device is operated inside an incubator at 37 °C with controlled CO_2 and humidity levels.

2.3 FEM modelling of the field and magnetic forces and torques

Finite element method modelling of the magnetic field created by the planar Halbach array was performed using COMSOL Multiphysics® software (COMSOL AB, Stockholm, Sweden, v. 6.3). The force $\boldsymbol{F}$ on a MD with magnetic moment $\boldsymbol{m}$, resulting from the magnetic induction field $\boldsymbol{B}$ gradient, is given by

$$\boldsymbol{F} = (\boldsymbol{m}\cdot\nabla)\boldsymbol{B} \tag{1}$$

In this calculation, we made the assumption that the magnetisation is saturated in the direction of the local field:

$$\boldsymbol{m} = m_0\frac{\boldsymbol{B}}{|B|}, \tag{2}$$

with $m_0 = 6.4 \times 10^{-14}\ A{*}m^2$.[40] The magnetic torque $\boldsymbol{T}$ acting on the particle is given by

$$\boldsymbol{T} = \boldsymbol{m} \times \boldsymbol{B}. \tag{3}$$

For this second calculation, we have considered the three situations where $\boldsymbol{B}$ is alternatively applied along the x, y or z direction.

2.4 Design of culture substrates

Culture supports were purchased from Cell&Soft. The soft supports, of 10 kPa stiffness, consist of a polyacrylamide hydrogel layer covalently attached to a glass coverslip and surface-coated with 1 μg cm^{-2} of fibronectin. Glass supports were provided with an identical coating of fibronectin. 10 kPa substrates containing fluorescent beads of 200 nm were also purchased to perform traction force microscopy (Cell&Soft, Mecatract). The growth surface available on the substrate was limited to a specific area where the cells experience a constant field amplitude (Fig. 2).

2.5 Cell culture and magnetic stimulation

The cell line used in this study is a GFP-tagged U87-MG purchased from ATCC. Cells were grown in Dulbecco's Modified Eagle's medium (DMEM, Gibco, ref. 31966047) completed with 10% fetal bovine serum (FBS, Gibco, ref. 10270106) and 1% ATAM (Gibco, ref. 15240062). Cells were cultured in a humidified atmosphere of 5% CO$_2$ at 37 °C. For the experiments, cells were seeded at a density of 4000 cells per cm^2 on the soft and the stiff substrates. The microdiscs were introduced into the culture plates 6 hours post-seeding at a concentration corresponding to 250 or 500 MDs per cell. The cells loaded with the magnetic particles were exposed to the magnetic field after 16 h of incubation. Cells were exposed to the field for 20 minutes, one condition right after the other. This consequently introduced a lag of 20 minutes between one and the other, which was taken into account during the cell assays. The field stimulation was performed at 37 °C in a humidified atmosphere of 5% CO$_2$. After the magnetic stimulation, the culture medium was changed to remove any detached cells.

2.6 Quantification of the number of particles per cell

The number of particles interacting with cells was quantified at three different nominal concentrations on the polyacrylamide and glass substrates *via* vibrating sample magnetometry, following the protocol described in ref. 32. A linear correlation between the areal concentration of particles and the number of particles interacting with cells was found in the range of concentrations studied (Fig. 3). The fitting function was used to adjust the nominal concentration to be added in the culture medium to obtain the desired number of particles per cell. Two particle loads were chosen for the experiments (250 and 500 MDs per cell) and correspond to areal concentrations of respectively 5 and 10 μg cm^{-2} for cells grown on the soft substrate and of 10.3 and 15.5 μg cm^{-2} for cells grown on glass.

2.7 Cell growth, death and motility assays

Cell counting and tracking were performed by live staining the nuclei with Incucyte Nuclight Rapid Red Dye (Sartorius, ref. 4717). The DNA stain was used at a dilution of 1 : 2000. It was added concomitantly with the magnetic particles. Cell death was quantified using propidium iodide at a concentration of 1 : 2000 (PI, Molecular Probes, ref. P3566).

After the magneto-mechanical stimulation, the cells were transferred to an inverted microscope equipped with a motorised stage (IX83 Olympus, Olympus France, Rungis, France) and an incubation chamber with controlled temperature, humidity and CO$_2$ pressure (Okolab, Rovereto, Italy). The cells were imaged at 10× magnification in five fields of view evenly distributed across the culture plate. Cell nuclei as well as PI-positive nuclei were counted 4 h and 24 h after the magneto-mechanical stimulation. Cell morphology was also quantified at these time points by capturing the green fluorescence of the cytoplasm. Cell motility was quantified by acquiring one image every 20 minutes for 3 h, beginning either 4 h or 24 h after the magneto-mechanical stimulation. The 20 minute time lag between samples imposed by the magnetic stimulation was taken into account in the implementation of the video time lapse. Since the time step is equivalent to the delay between one stimulation and the other, by carefully choosing the start and end frame of the three-hour sequence, we were able to extract a 2 hour time lapse that starts at scheduled times of 4 h and 24 h for each condition. A control condition corresponding to cells with MDs not subjected to a field was included for both types of substrates.

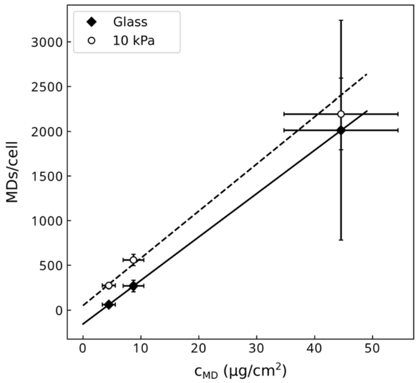

Fig. 3 Relationship between the concentration of microdiscs (MDs) delivered in the culture medium and the number of microdiscs interacting with the cells.

2.8 Image analysis

The nuclei of Nuclight positive cells were segmented with a trained Cellpose model.[41] The training was implemented starting from the cyto2 pre-trained model, as described in ref. 32. The cell number was obtained from the segmented masks with an in-house Python 3 script, summed over all fields of view, and normalized to the control condition, consisting of cells loaded with MDs but not exposed to the magnetic field. Given the low number of PI positive cells and the low contrasted signal, CY3 positive cells were counted manually over all the fields of view. The proportion of dying cells was obtained by calculating the ratio of this number relative to the total cell number. Motility was determined by tracking the nuclei of Nuclight positive cells. As described above, the nuclei were segmented with the trained Cellpose model. The ImageJ TrackMate plugin[42] was applied to the segmented images. For each stack, the velocities at every step were pooled together, regardless of the cell trajectory they belonged to. The median velocity was calculated from the pooled data set. The mean of the medians was then calculated for every condition.

Changes in cell morphology were quantified by measuring the intensity of fluorescence of the cytoplasm of the GFP-tagged U87-MG. When a cell shrinks, the intensity level per pixel increases since it is the projection of the volume concentration of the GFP. To conduct this analysis, the GFP images were segmented using a Cellpose-trained neural network. The network was trained in a similar way to that used for nuclei detection. The raw GFP images were then multiplied by the binarised mask to obtain the distribution of intensities of every pixel belonging to cell bodies. This distribution was corrected by the background signal as follows: the mask was inverted and multiplied by the raw image. The median intensity of the resulting image was calculated. The median background intensity was subtracted from the cell intensity distribution. This correction was applied frame-by-frame. Negative values were filtered out.

2.9 Immunofluorescence and confocal imaging

Two hours post-field stimulation, the cells were permeabilised for 15 min in a solution of $PBS^{+/+}$ containing 4% PFA and 0.5% Triton 100x. They were then fixed with a solution of 4% of PFA in $PBS^{+/+}$ for 45 min. The permeabilisation step allowed a significant decrease in the fluorescence levels of the GFP in the cytoplasm of the cells and the Nuclight stain. Vimentin was stained with a mouse monoclonal antibody (Vimentin V9 Ref. sc-6260, Santa Cruz Technology) at dilution 1 : 50 and a goat anti-mouse CY2 secondary antibody (Jackson Immunology, ref. 115225146) at 1 : 200 dilution. Actin was stained using Alexa Fluor Plus 647 Phalloidin (Invitrogen, ref. A30107) at 1 : 400 dilution following the provider's recommendations. Finally, the nuclei were stained with Hoechst 33 342 at 1 : 1000 dilution. These concentrations of antibodies yielded a signal that strongly dominates the remaining fluorescence of the cytoplasm and of the Nucligth stain.

The stained samples were imaged with confocal microscopy (LSM 880, Zeiss) at either 63× or 40× magnification, using oil immersion objectives. In-depth images of the samples were acquired with a spacing of 0.3 μm. MDs were imaged at the same altitudes using reflected light at 488 nm.

2.10 Traction force microscopy

Cells were seeded at 4000 cells per cm^2 on the polyacrylamide hydrogels designed for traction force microscopy (TFM). Image acquisition was performed using a 60× oil immersion objective (NA 1.4) 2 h and 5 h after the cells have been exposed to the magnetic field, or, for the control condition, 26 h and 29 h post-seeding. Stacks of images of the fluorescent beads were acquired in the vicinity of the surface of the hydrogel with 0.3 μm spacing in order to compensate for any vertical drift of the surface. In parallel to capturing images of the fluorescent beads, phase contrast and GFP images were captured to visualise the cells and the MDs. The latter appear either black or bright green on the GFP images when in contact with cells, while they are more visible on phase contrast images, when they lie in the surrounding area. At the end of the experiment, the cells were detached using 0.5% trypsin-EDTA (Trypsin-EDTA 10 x, Gibco, Thermo Fisher Scientific, Gennevilliers, France, ref. 15 400) for one hour. This allowed imaging of the relaxed state of the gel or reference state.

The quantification of the hydrogel deformation field is detailed in a previous publication.[43] In brief, the deformation field is obtained by measuring the displacement of fluorescent beads located in the close vicinity of the surface. This is achieved by comparing the bead positions while the cell is present and pulling on the gel, the strained state, to the cell-free hydrogel, the reference state. A reference image is selected from the reference stack, which is the closest to the surface of the gel. A home-made registration algorithm was used to compensate for the in-depth and lateral drifts of the strained image by comparing the bead positions in regions of the strained state that are far from the cells (and therefore where a reduced deformation of the substrate is expected) to the reference image. Once the images were corrected for drifts, the deformation field was quantified using the Kanade–Lucas–Tomasi pyramidal optical flow algorithm, as described in ref. 43. Between 45 000 and 52 000 fluorescent beads were tracked on images whose size is of the order of 2000 × 2000 pixels. Four levels in the pyramid were used, thus working with subsampling the original image with new pixel sizes of respectively 64, 16, 4, and 1 times the original pixel area. The sizes of the interrogation windows used to track the displacements were respectively 40^2, 30^2, 20^2, and 20^2 pixels, with the unit pixel size referring to that of the level of the pyramid. The calculation of the force field was performed using Fourier transform traction cytometry.[44] The noise level of the traction forces was quantified from the force field out of the cells (Fig. S1). To do so, masks were drawn based on the GFP and phase contrast images to differentiate the cell body from the background. Since U87-MG cells tend to overlap and form small groups, the forces were analysed per field of view and not per cell, as it was not possible to single out individual cells within colonies. Then, a mask of areas devoid of MDs and cells was drawn for each image and the distribution of forces out of cell bodies and adhered particles was calculated. The 0.025 and 0.975 quantiles of the distribution of the *x* and *y* components of the traction stresses were calculated. The upper value of the quantile was used to filter the data measured in cells: only values that exceeded this threshold were used for further analysis. An example of this filtering process is reported in supplementary Fig. S1.

2.11 Statistical analysis

Every assay was performed in triplicate, with cells coming from different passages in order to yield three independent experiments ($n = 3$). The mean and standard deviations were calculated over these three values.

One sample Student's *t*-tests compared to 1 were used whenever we calculated ratios or normalised values (cell detachment or proliferation), with a 0.05 significance level to reject the null hypothesis. As we expect the magnetic stimulation to damage cells, we used one-tailed *t*-tests to test the null hypothesis when comparing the positivity of PI-staining in cells that have been stimulated by the magnetic field to the control, unstimulated cells. Similarly, one-tailed Student's *t*-tests were used to assess the significance of the contribution of MD vibration to the increase in the proportion of PI-positive cells compared with the 0 Hz condition. In all other cases, two-tailed Student's *t*-tests were used. One-way ANOVA tests were used to assess any variation with frequency. For all tests, a significance level of 0.05 was chosen to reject the null hypothesis.

For the analysis of morphological changes, the corrected distributions of pixels values were pooled between the three independent experiments, condition per condition. The cumulative distribution function (CDF) was then calculated over the whole set of data.

Regarding the motility measurement, the median velocity per condition was calculated from the distribution of velocities of every cells displacement in each independent experiment. Means of the medians were used to asses any statistical difference with the control using two-tailed *t*-tests, as previously described. The data of the three experiments were then pooled to calculate the general distribution per condition.

To evaluate any significant difference in cellular traction forces between conditions, the median values of the filtered distribution of the cellular traction forces was calculated per field of view. The mean of the medians was then calculated per experiment. Two-tailed *t*-tests were used to compare to the control condition, consisting of cells loaded with MDs but not exposed to the magnetic field. Moreover, the distribution of filtered force amplitudes was pooled by condition to calculate the associated CDF.

3 Results

3.1 The magnetic particles exert oscillating torques and compressive forces when actuated by a rotating Halbach array

Using FEM, we calculated the magnetic torque that arises when a magnetisation is submitted to the oscillating field (Fig. 4). This models a MD that is immobilized, and whose

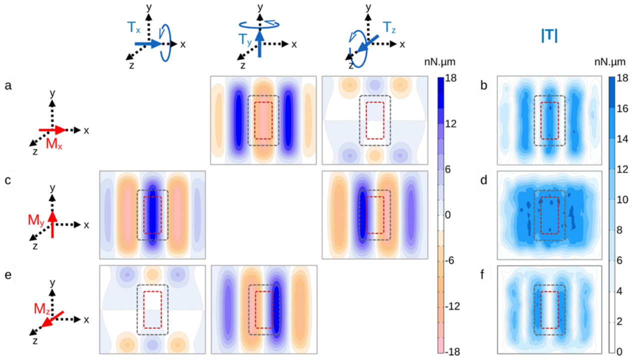

Fig. 4 2D maps of the magnetic torques applied by the Halbach array to immobilised particles positioned 4 mm above the magnets and whose magnetisation is saturated. The maps are organised in a table. Different orientations of the magnetisation, illustrated by a red arrow on the schematics on the left of the table, are shown in rows. The blue arrows in the schematics on top of the table illustrate components of the rotational motion possibly induced by the magnetic torque $\boldsymbol{T}$. The last column shows $|\boldsymbol{T}|$, the amplitude of the torque vector. (a and b) The magnetisation is oriented along the *x* axis. (a) Components along *x*, *y* and *z* axes and (b) amplitude of the magnetic torque. The torque is predominantly aligned along the *y* axis. (c and d) Same with the magnetisation being oriented along the *y* axis. In this geometry, the torque components along the *x* and *z* axes have similar amplitudes. (e and f) Same with the magnetisation being oriented along the *z* axis. The torque is predominantly aligned along the *y* axis. The red and the grey dashed rectangles show the regions of interest, resp. in the static regime and when the array is set in orbital motion.

magnetisation is saturated and remains so under field oscillations. As the torque value depends on the relative orientation between the MD magnetisation and the local magnetic field, we have considered the three limiting cases where the saturated magnetisation is along the *x*, *y* or *z* direction. Focusing on the central region of the array where the cells are grown, the largest torques are experienced when the MD magnetisation is within the *xy* plane, with an amplitude of about 15 nN µm (Fig. 4b and d). Vertical-pointing magnetisation along the *z*-axis results in a much reduced magnetic torque (Fig. 4f). Because the MDs are highly anisotropic in shape, the magnetic torque $\boldsymbol{T}$ only transfers into a mechanical torque when it is parallel to the flat plane of the particle, the *xy* plane. For instance, T_z torque induces magnetisation rotation within the *xy* plane, but no mechanical torque. Considering now the orbital motion of the magnets in the *xy* plane, the simulation shows that it induces either a variation in the magnetic torque amplitude when the particle is saturated along the *x* or the *z* axis or a transfer of the torque from the *x* to the *z* axis while keeping its amplitude fairly constant when the particle is saturated along the *y* axis (Fig. 4). This simulation also indicates that the order of magnitude of the torque is in the nN µm range and therefore is sufficient to reorganise and alter the cell cytoskeleton[45] or disrupt cell membrane,[46] but not sufficient to induce a thermal effect.[40]

In addition to the magnetic torques, the finite element computation also shows that the Halbach array exerts forces on the MD. As shown in Fig. 5, the forces in the *xy* plane are below 1

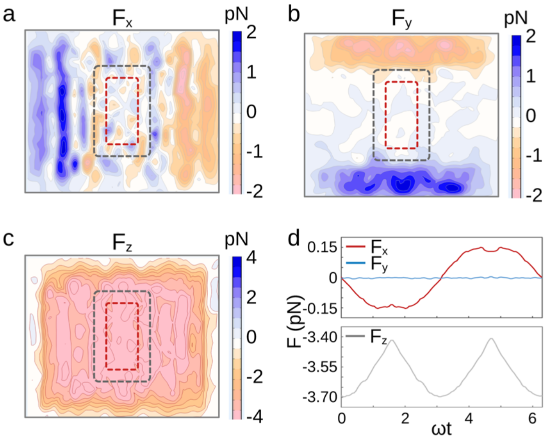

Fig. 5 (a–c) 2D maps of the translational forces on particles with saturated magnetisation along the local field. The particles are positioned 4 mm above the magnets. The red and grey dashed rectangles show the regions of interest, resp. in the static regime and when the array is set in orbital motion. (d) Time variation of the translational forces for a particle positioned at the center of the red dashed rectangle and saturated along the x-direction. ω is the pulsation of the orbital movement of the array of magnets.

pN. On the other hand, the vertical, downward force is larger (about 3.5 pN). Such a force amplitude can be expected to trigger ion channel opening, but is not sufficient to rupture membranes.[47] However, the actual forces might exceed the values reported here in the case where particle aggregation occurs in cells. These clusters are expected to give rise to forces of larger magnitude, in proportion to the number of particles in the aggregate. Field-induced translational forces could then become sufficient to provoke cellular damage, such as impairment of the integrity of the cytoskeleton or disturbance of protein assemblies.[48]

3.2 At equal particle loads, a soft extracellular environment enhances the adverse effect of stimulation over cell detachment, viability and proliferation

U87-MG cells were first exposed to the magnetic microdiscs at a concentration such that the cells are loaded with an average of 500 particles per cell. Since cells grown on a stiff or on a soft substrate do not capture the same amount of microdiscs,[32] the volume concentration of particles was adapted to each condition (see Materials and Methods). In previous work, we have shown that this concentration of microdiscs does not significantly alter the viability of U87-MG cells on both substrates.[32] The cells were then exposed to a magnetic field of amplitude 250 mT. The frequency of the rotation of the Halbach array was assayed between 0 Hz (static field) and 10 Hz.

While these stimulation conditions do not impact cell behaviour in the absence of microdiscs[15,17] (Fig. S2), they may cause an increase in cell death and a decrease in proliferation (Fig. 6, one-way ANOVA test on respectively gel and glass (b) $p = 0.02, 0.005$, (c) $p = 0.03, 0.25$, and (d) on gel $p = 0.01$). Indeed, Fig. 6 shows that the magneto-mechanical stimulation has more adverse effects in cells grown on the soft substrate. For instance, a significant proportion of cells (about 40%) detach from the soft support 4 h after the 10 Hz, 20 min long magnetic stimulation (Fig. 6a) ($p = 0.01$). This is in contrast to glass ($p_{\text{glass}-10\text{kPa}} = 0.01$), where all the cells remain adhered. Similarly, the loss of viability is more pronounced in cells grown on a 10 kPa substrate than on glass (Fig. 6b and c) (2-way ANOVA test 4 h post-stimulation: $p = 0.01$). Nevertheless, field application has an effect under both culture conditions. In particular, we note that exposure to a static field alone for 20 min (0 Hz) triggers an increase in the number of cells entering death processes in the first hours following the stimulation ($p = 0.01$ (glass), $p = 0.02$ (10 kPa)). A superimposed alternating field leads to additional significant damage, but only in cells grown on the 10 kPa support ($p = 0.03$ at 10 Hz). This effect persists 24 h after the field has been released (Fig. 6c, $p = 0.02$). This is in contrast to glass, on which setting in vibration microdiscs that exert a static pressure does not induce additional alteration in cells compared to a stimulation consisting of a static pressure only ($p = 0.5$ at 10 Hz). Finally, we observe that the magnetic stimulation halts cell proliferation, but again this happens only on the soft substrate (Fig. 6d, one-way ANOVA on 10 kPa: $p = 0.01$; one sample t-test respectively on glass and 10 kPa: $p = 0.001, 0.007$ (Ctrl), $p = 0.03, 0.23$ (0 Hz), $p = 0.0008, 0.13$ (2 Hz), $p = 0.01, 0.11$ (10 Hz)).

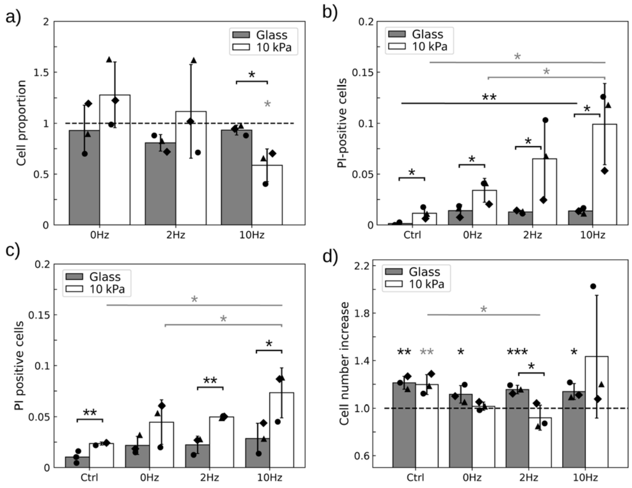

Fig. 6 Field application perturbs cells more when grown on a 10 kPa substrate. (a) Proportion of remaining cells respective to control 4 h after field application at 3 different frequencies, for the two substrates: glass and 10 kPa polyacrylamide hydrogel both coated with 1 μg cm^{-2}. (b–c) Application of the magnetic field increases the proportion of PI-positive cells (b) 4 h and (c) 24 h after field application. Vibrating particles have a significantly stronger detrimental effect than those submitted to a static field on the soft substrate. (d) Cell proliferation is halted after field application in cells grown on a 10 kPa substrate, in the presence of either a static or an oscillating field. Black symbols show independent experiments ($n = 3$). Error bars represent the standard deviation of the means. *, **, and *** denote significance with respectively $p < 0.05$, 0.01, and 0.001. Gray stars refer to statistics for the soft substrate condition while black stars refer to the glass substrate. Only significant differences are labelled.

As a whole, we conclude that U87-MG cells loaded with an average of 500 MDs per cell are more affected by the magnetic stimulation when they are grown on a physiologically soft substrate than on a substrate with an out-of-physiology stiffness. The magnetic actuation of the MDs results in cell detachment, a halt in cell proliferation and loss of viability. An important observation is that while the static field, and the resulting vertical pressure exerted by the particles, is enough to induce damage in the cells, vibrating particles trigger additional detrimental effects that are only visible in cells grown on soft substrates although the average load of particles per cell is identical under both culture conditions.

3.3 At lower particle load, cells grown on 10 kPa exhibit significant frequency-dependent halt in proliferation and transient reduction in viability and motility

Our goal then is to better understand how the actuated particles may alter normal cell fate. Loading cells with an average of 500 MDs leads to cell detachment for cells grown on the soft substrate (Fig. 6a). This inevitably results in cell selection, with only the least particle-laden cells or the most robust phenotypes being selected. This selection then influences and may bias subsequent cell viability or proliferation experiments. Indeed, we observe that the dispersion of the data is much larger in the experiments conducted on the soft substrate than on glass where the cell number does not decrease after treatment. We attribute this difference to the selection in favour of the cells least affected by the mechanical disturbance. As detachment may depend on the state of the neighbouring cells and therefore on the local cell density, the state of the remaining cells is likely to be more variable. We confirmed this hypothesis by comparing the dispersion in the proportion of PI-positive cells throughout the substrates in each independent experiment (Fig. S3).

When the load is reduced to 250 particles per cell, the stimulation does not induce significant cell detachment, thus avoiding selection of specific phenotypes (Fig. 7a, $p > 0.3$ for all conditions). Then, we can evaluate the impact of the magnetic stimulation on the heterogeneous cell population, loaded with variable numbers of particles as would occur under conditions where cells cannot be discarded from the experiment (like *in vivo*).

With this lower dose of MDs, we thus report on the response of the whole cell population, having a heterogenous load of particles and therefore variable intensities of perturbation. Fig. 7b shows that 4 h post-treatment, cell viability is significantly altered at all frequencies, including the static treatment (0 Hz). Although the effect seems to increase with frequency, a frequency-dependence could not be assessed due to the large variability in cell responses (one-way ANOVA: $p = 0.13$). Nonetheless, the frequency of the treatment has a significant impact on cell proliferation (Fig. 7c). Proliferation is impaired only when the particles vibrate: with this load of particles, static compression (0 Hz) is not sufficient to alter this function, although 20 min of vibration at any of the assayed frequencies does. Similarly, cell motile capabilities decrease when the particles are stimulated by the magnetic field (Fig. 7d, one-way ANOVA: $p = 0.008$). But this decrease is only significant relative to the control when the particles vibrate, not under static stimulation ($p = 0.06$ (0 Hz), 0.01 (2 Hz), 0.005 (10 Hz), and 0.001 (20 Hz)). Nevertheless, the impact of the mechanical stresses exerted by the particles on cell viability and motility decreases in time. None of these read-outs remained significant 24 h post-treatment. Thus, we conclude that the most obvious persistent effect of the stimulation is to stop cell proliferation for at least 24 h.

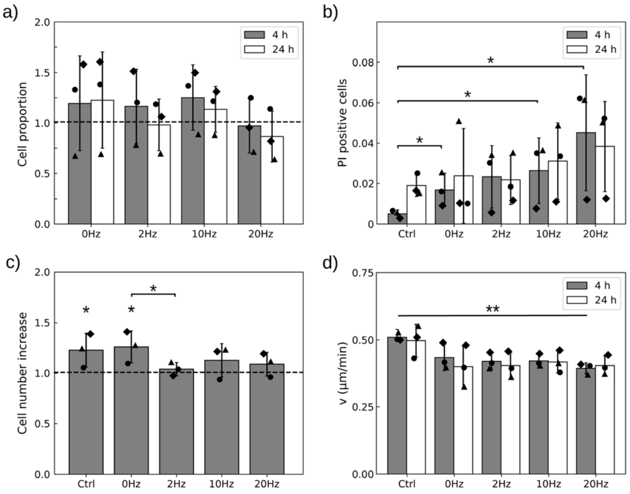

Fig. 7 With a mean load of 250 MDs per cell, field application alters cell viability, proliferation and motility. (a) Cells remain attached to the 10 kPa substrate when treated with a static pressure (0 Hz) or vibrating particles. The proportion is calculated relative to the control in the absence of a field. (b) The proportion of PI-positive cells increases 4 h but not 24 h after field application relative to the control. (c) Cell proliferation is halted after field application in cells submitted to an oscillating field but not a static one. (d) Cell migration is on average slowed down 4 h after the treatment but recovers 20 h later. Black symbols show independent experiments ($n = 3$). Error bars represent standard deviations of the mean (a–c) of median (d) values. * and ** denote significance with respectively $p < 0.05$ and 0.01. Only significant differences are labelled.

3.4 Cell morphology on a soft substrate is persistently altered at both microdisc loads assayed but only when vibrated

As shown above, mechanical perturbations of the cells by the actuated MDs have consequences whose persistence in time depends on the cellular function considered. The ones we focused on, viability, proliferation or migration, are key concerning cancer evolution but they result from the integration of many highly regulated biochemical reactions. In contrast, cell shape is a lower level read-out in terms of biological complexity, which can be predictive of cell outcome.[49] We therefore focused on cell morphology and analysed how the mechanical perturbation would impact it. By carefully looking at cell shape dynamics, we observed that under some conditions, after an immediate collapse, some cells were spreading again a few hours later (Fig. 8a). We took advantage of the fluorescence of the GFP tagged U87-MG cells to quantify the change in morphology, as collapsed cells exhibit a larger fluorescent signal per pixel (Fig. 8b). We therefore measured the fluorescent signal of every pixel associated with a cell and plotted the

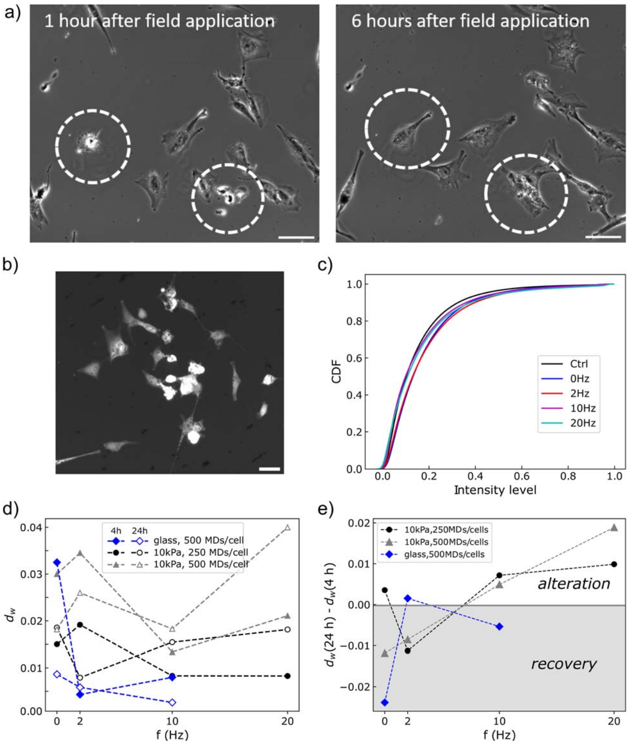

Fig. 8 (a) Cells undergo morphological changes due to the field-induced particle actuation, collapsing to a round shape. The morphological change is reversible when the cell is not dying, as highlighted by the cells inside the dashed circles. Scale bar: 100 μm. (b) The shrinkage of the cells causes an increase in the fluorescence of the pixels in the cell coming from the reduced volume. Scale bar: 50 μm. (c) Cumulative distribution function (CDF) of the fluorescence intensity per pixel of the cells 4 h post-treatment, when the cells are grown on a 10 kPa substrate and are loaded with 500 MDs per cell. (d) Wasserstein distance (d_w) between control conditions and cells submitted to the magnetic field measured 4 h or 24 h post-treatment, for different culture conditions (glass and 10 kPa substrate) and densities of MDs (250 or 500 MDs per cell). (e) The variation of the Wasserstein distance in time provides information on the evolution of cell morphology compared to control.

cumulative distribution function (CDF) of the normalized, background-corrected intensity. An example of such a cumulative function is shown for cells grown on the soft substrate, bearing an average load of 500 MDs per cell and observed 4 h after magnetic stimulation (Fig. 8c). It shows that after stimulation, the intensity of fluorescence is shifted toward larger values compared to the control condition, meaning that cells have adopted a more rounded morphology. Under all conditions, we observed that the CDF departs from the control condition toward larger fluorescent intensity (Fig. S4). We quantified this observation by calculating the Wasserstein distance (d_w) between the control condition (particle-laden cells unexposed to the magnetic field) and those submitted to a static or alternating field, for cells grown on glass or on the 10 kPa substrate (Fig. 8d). On glass, a narrower frequency range, from 0 Hz to 10 Hz, was spanned, as we had not observed any frequency-dependent loss of viability or proliferation (Fig. 6). The Wasserstein distance provides here a metric of the integrated distance between the two CDFs. Comparing the Wasserstein distances calculated 4 h and 24 h post-treatment allowed assessment of whether the cells recover a morphology closer to the control or evolve toward an even more rounded shape, *a priori* associated with dying processes (Fig. 8e). As a whole, this analysis highlights that the shape of cells grown on the soft substrate is persistently altered when they are exposed to a 10 Hz or 20 Hz stimulation, at the two doses of MDs assayed. This is in contrast to glass where the Wasserstein distance decreases in time at 10 Hz, suggesting that the cells recover progressively their morphology.

Fig. 8d also shows that the static field has a short term impact on cell morphology under all culture conditions, which is more pronounced at larger concentrations of MDs, consistent with the fact that the static field generates a downward mechanical pressure whose amplitude is proportional to the number of particles per unit surface. Nevertheless, we observe that the morphology of cells grown on glass evolves toward their unperturbed morphology faster than those grown on the soft substrate at equal particle load (Fig. 8e). The evolution of the Wasserstein distance with frequency seems to be non-monotonic under all conditions and differs between cells grown on glass or on the soft substrate (Fig. 8d). For instance, the addition of a mechanical vibration at 2 Hz seems to have a large initial impact on cell morphology in cells grown on the soft substrate, but the cells progressively recover a spread morphology a few hours later. This is in contrast to the effects of vibrations at 10 Hz or 20 Hz, which appear more persistent.

3.5 The microdiscs interact with the actin and vimentin cytoskeletons

We observed that cell morphology is differentially altered as a function of the stiffness of the substrate and the frequency of the mechanical perturbation. Cell shape closely relates to the organisation of the cytoskeleton, which differs whether cells are grown on a soft or a stiff substrate[50,51] (Fig. S5). We therefore questioned whether the mechanical vibrations of the particles, which enhance the detrimental effects of particle actuation on cell viability, proliferation or migration compared to a compressional stress alone, could lead to visible damage of the cytoskeleton organisation.

In previous studies,[11,32] we and others have shown that in the absence of surface functionalization, MDs are internalised in cells. TEM imaging[11] as well as DIL staining[32] did not highlight any membrane around the particles, suggesting that they could enter the cell body through a translocation process.[52] Indeed, many of them can be seen in the cytoplasm of the GFP-tagged U87-MG cells (Fig. S6). We thus imaged the actin and the vimentin cytoskeletons of cells loaded with an average of 250 MDs that had been submitted to a compressional stress alone or a combination of compressional and vibrational stresses. Both cytoskeletons were immuno-stained 24 h post-treatment and compared to particle-laden cells that were not exposed to the magnetic field (Fig. 9).

Confocal imaging provided some information on the localization of the MDs relative to the cytoskeleton. We observed that

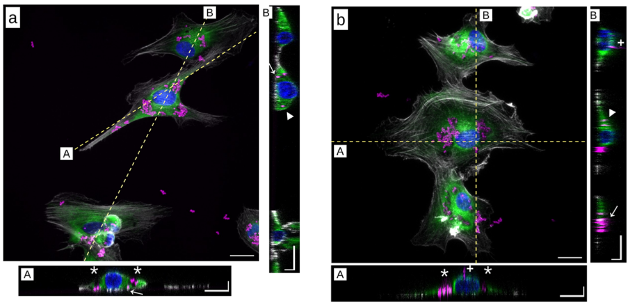

Fig. 9 Representative snapshots of immunostained U87-MG cells exposed to the microdiscs for 24 h in the absence of a magnetic field. The cells are grown on (a) glass or on (b) a 10 kPa substrate. Actin is shown in grey, vimentin in green and nuclei in blue. Bottom and right hand side panels show in-depth cross sections of cells acquired along the labelled dashed lines. The white stars point toward microdiscs trapped in void regions of the vimentin cytoskeleton. The white triangles (resp. arrows) point toward particles embedded into the vimentin (resp. actin) cytoskeleton. Plus (+) symbols show microdiscs bound to the membrane. In-plane bar: 20 µm. In-depth bar: 5 µm.

the particles are positioned either at the cell membrane, into the vimentin network or in contact with actin fibres, or that they are trapped into vacuoles devoid of vimentin and actin that are presumably related to autophagy (Fig. 9). Of note, U87-MG cells are cancer cells with highly active autophagy processes even in the absence of particles.[53] We confirmed that these vacuoles embedded into the vimentin cytoskeleton are also found in the absence of particles, although they are more frequent in their presence (Fig. S5). A slight depletion of actin filaments was observed in cells exposed to a 10 Hz stimulation, while no depletion was visible in the vimentin cytoskeleton (Fig. S7). No such actin depletion was visible in the control condition. Nevertheless, these events were rare and hardly visible. They could not be quantified to conclude about a differential alteration of the actin cytoskeleton when the frequency is varied.

3.6 The vibrations of the microdiscs alter cell contractility

The optical analysis of the actin and vimentin cytoskeletons provides us information on the location of the particles relative to them but this analysis lacks resolution to conclude about the impact of the vibrational movement of the particles on their integrity. For this reason, we quantified the mechanical stresses the cells exert on the substrate. These stresses provide information on cell contractility,[54] a read-out of the integrity of the cytoskeleton.

We conducted this analysis by both looking at the cell-averaged contractility and the subcellular force patterns. We compared the contractility of cells loaded with an average of 250 particles per cell and exposed to static (0 Hz) or alternating fields (2, 10, 20 Hz) to two control conditions: MD-free cells and MD-laden cells, both in the absence of a magnetic field (Fig. 10). The control without particles was performed to identify a potential perturbation of cellular forces coming from the internalised particles, in the absence of a magnetic field.

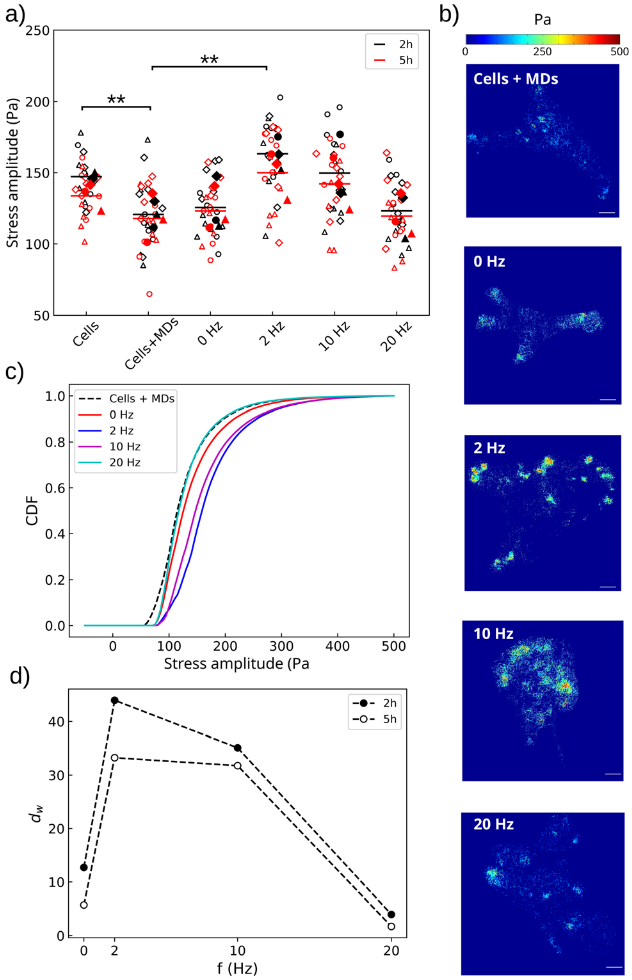

Fig. 10 The mechanical stimulation enhances cell contractility. (a) Amplitude of the cellular stresses transmitted to the substrate. Empty symbols show median values for each field of view, while filled symbols are the mean of the medians per experiment. Different shapes indicate independent experiments ($n = 3$). The horizontal bars are the means of the replicates. Significance was calculated against the control condition cells + MDs with a two-tailed t-student test. Black (resp. red) colour shows results and statistics 2 h (resp. 5 h) after stimulation. ** denotes significance with $p < 0.01$. Only significant differences are labelled. (b) Representative traction force patterns, 2 h post-treatment. The control condition consists of particle-laden cells not exposed to the magnetic field. Scale bar: 25 µm. (c) Cumulative distribution function (CDF) of the stress amplitude for the different mechanical perturbations. (d) The Wasserstein distance (d_w) shows that the 2 Hz and 10 Hz treatments have the greatest impact on cell contractile capabilities, but that this impact tends to decrease in time.

Amplitude maps of the mechanical forces per unit surface transmitted by the cells to the substrate were calculated from the displacements of nano-scaled fluorescent polystyrene beads embedded into the hydrogel substrates, as described in Materials and Methods. The stress map was restricted to the inside of the cellular contour. The outer signal, with the exception of that coming from non-internalised magnetic MDs lying on the substrate, was used to determine the noise level of the measurement. The inner signal could thus be filtered and only stresses above the noise level were considered (Fig. S1). Data were acquired 2 h and 5 h after magnetic stimulation to analyse the immediate evolution of cellular forces following the mechanical perturbation.

We first observed that in the absence of magnetic stimulation, cells having no particles inside exert significantly larger stresses than those loaded with 250 particles per cell (Fig. 10a, $p = 0.008$). This evidences that although the MDs were shown to be inert concerning cell metabolic activity, viability, proliferation or migration at this dose of particles,[32] they do perturb a very basic regulator of many cellular functions, the contractile machinery. Secondly, while we do not observe any significant variation of the cellular stresses after the particles have exerted a static compression ($p_{0\text{Hz}} = 0.71$), we observe that the 2 Hz treatment results in a significant increase in the amplitude of the stresses compared to the control situation of cells loaded with MDs ($p_{2\text{Hz}} = 0.008$). An increase in the frequency of the vibration however leads to a less significant outcome, which was completely lost at 20 Hz ($p_{10\text{Hz}} = 0.11$ and $p_{20\text{Hz}} = 0.83$). This suggests that the vibrations of the MDs only alter cell contractility in a narrow range of frequencies, on the order of a few Hz. Looking at the median values of the traction forces, the perturbation appears transient, with the effect no longer significant 5 h post-treatment ($p_{2\text{Hz}} = 0.08$ and $p_{10\text{Hz}} = 0.16$ and $p_{20\text{Hz}} = 0.90$). However, analysing the median values alone might lead to incomplete results, given the difference in the distribution of the force points through the cells after they were submitted to an alternating field or not (Fig. 10b). Large amplitude traction points were often observed in cells submitted to the stimulation, in contrast to the control. This qualitative observation was made more quantitative by comparing the cumulative distribution function of the force amplitudes (Fig. 10c). Consistently, we observed a positive shift of the CDFs at 2 and 10 Hz relative to the non-stimulated cells loaded with MDs, meaning that these two conditions generate local forces of larger amplitude. In contrast, the 20 Hz stimulation did not induce any change in the amplitudes of the local cellular stresses compared to those of the control condition. Calculation of the Wasserstein distance relative to the non-stimulated control condition additionally showed that the alteration in cell contractility persists 5 h post-treatment but only when the cells are stimulated with 2 Hz or 10 Hz (Fig. 10d).

4 Discussion

Previous studies using conventional 2D culture plates have demonstrated that low-frequency, field-induced vibration of micrometric disc-shaped particles can elicit cell death at remarkably high rates, ranging from 60% to 90%.[13,15,17,55] Notably, Kim *et al.*[13] and Leulmi *et al.*[55] functionalised these discs to target the cell membrane, achieving comparable results with two different cancer cell lines, glioblastoma and renal tumour respectively. The initiation of apoptotic pathways was attributed to an elevated influx of calcium ions, driven by the magnetic-induced stimulation.[13] Additionally, studies have reported instances where internalised particles, when actuated, trigger cell death in the glioblastoma cell line U87-MG,[15,17,56] suggesting the potential of this approach for innovative anti-cancer therapies. However, translating these promising *in vitro* findings to more complex environments, such as 3D artificial scaffolds or *in vivo* models, has proven challenging.[15,25,26] Among the factors differentiating conventional culture substrates from 3D substrates and *in vivo* tissues, the mechanical properties of the extracellular environment are particularly significant. Notably, culturing cells on 2D soft substrates has been shown to better preserve cell phenotypes and enable transcriptomic expression profiles that closely resemble those observed *in vivo*.[36]

Motivated by the discrepancies in cell outcomes observed between conventional plastic plates and more biomimetic environments, this study examines the role of extracellular matrix softness in shaping cell fate following the actuation of magnetic microdiscs. Specifically, we seek to determine whether the mechanical properties of the extracellular environment modulate the cellular response to the microdisc-induced mechanical perturbations. Our experimental setup involves superimposing compressive forces and shear stresses coming from particle actuation. The soft extracellular environment is mimicked using a 50 μm-thick layer of polyacrylamide hydrogel coated with fibronectin, a protein of the extracellular matrix. This stiffness is representative of the core of solid glioblastoma tumour, although it does not consider stiffness heterogeneity produced by the extensive fibrotic-like ECM remodelling, which results in peritumoral stiffness values between 0.3 and 10 kPa.[28] Glass substrates coated with the same amount of fibronectin serve as controls for conventional 2D culture. This protocol enables the discrimination of the impact of the extracellular matrix softness from other cues, such as chemical interactions of the cells with the surface.

Here, we employed the U87-MG cell line, a well-established *in vitro* model of glioblastoma cells. The response of these cells to intracellular particle actuation has been analysed in several former studies, using conventional culture plates.[13,15,17,56] They all concluded that vibrating particles are effective in inducing cell death. When performing similar analysis with cells grown on a soft substrate (10 kPa), our main observation is that the cells are even more sensitive to the magneto-mechanical stimulation compared to those grown on stiff substrates. This suggests that even when used at a non-toxic dose, the particles may trigger significant responses in cells grown on substrates with physiologically relevant mechanical properties at lower doses than previously anticipated in plastic plates. While the majority of the literature on vortex microdiscs has focused on glioblastoma, the agreement with the findings of Leulmi *et al.*[55] indicates that similar trends could also be present in other tumour models.

More specifically, our first key finding is that the mechanical perturbation exerted by the static pressure of the MDs is sufficient to induce cell death and limit proliferation, with this effect being more pronounced in cells grown on a soft substrate (Fig. 6). Our second key finding is that superimposing vibration onto the compressive force significantly enhances treatment efficacy in cells grown on the soft substrate, unlike those grown on glass (Fig. 6). Although it was not possible to assay vibration alone in this setup, the lack of a significant difference in cell death rates between static compression and combined compressive and vibrating stimulations at a lower dose of MDs (Fig. 7) suggests that both stimulations play complementary roles in compromising cell integrity.

A plausible mechanism underlying this phenomenon is that the compressive forces exerted by the particles in the cell body impair the integrity of cellular membranes and the cytoskeleton. This is supported by our observation that the MDs interact with both cell compartments[32] (Fig. 9 and S7). As demonstrated by Kim *et al.*, membrane bending may activate mechanosensitive ion channels, initiating cell death programs.[13] Additionally, compressive stresses in the order of tens of kPa (nN μm^{-2}) can rupture the cell membrane,[46] a range achievable when several hundred MDs aggregate. Similar compressive forces are also in principle sufficient to alter the integrity of membrane-bound organelles such as autophagosomes and lysosomes, leading to the release of their acidic content.[57]

The differential response of cells grown on a soft or a stiff substrate may be attributed to the softer rheological properties of cells grown on soft substrates.[58–60] This is associated with a reduced content of actin stress fibres[61] (Fig. S5). The adaptation of actin cytoskeleton organisation to the stiffness of the extracellular matrix is well-documented[62–64] and correlates with changes in cellular rheological properties.[65] In our study, as the MDs are internalised by the cells (Fig. 9), their motion is constrained by the mechanical properties of the cell interior, with stiffer compartments impeding particle vibration.[40] This may explain why adding vibration to the compressive force has no additional effect on cells grown on glass, whereas on the 10 kPa substrate, vibration significantly enhances cell death and detachment (Fig. 6). Another factor contributing to the resilience of cells grown on hard substrates to mechanical perturbations is the different organisation of vimentin intermediate filaments and their interactions with actin and microtubule cytoskeletons. The vimentin cytoskeleton exhibits visco-elastic properties.[66] It thus dissipates mechanical energy[67] and provides mechanical support to various cellular functions, such as trafficking and adhesion.[68] Moreover, vimentin can directly cross-link to actin and microtubules and stabilise them.[63] Finally, vimentin is upregulated in cells grown on stiff substrates,[61] which may provide additional protection to the cells against intracellular mechanical perturbations. Consistently, we qualitatively observe separated vimentin and actin cytoskeletons in cells grown on the 10 kPa substrate, while they are intertwined in cells grown on glass (Fig. S5). Since the sensitivity of cytoskeletal organisation to the surrounding mechanical environment is not specific to glioblastoma cells, we expect that similar behaviour may extend to other cancer cell types, with of course some variations depending on the specific cell type.

Soft substrates, by allowing the translation of MD forces and torques into noticeable deformation of intracellular compartments, thus appear as an interesting platform to study the influence of local mechanical vibrations in cells grown in mechanically relevant environments. Working with a reduced load of 250 MDs per cell on average allowed the limitation of cell detachment and phenotype selection. At this load, we observe that the static pressure exerted by the particles is sufficient to transiently alter cell viability and morphology, but not proliferation or motility (Fig. 7 and 8). In contrast, superimposing a vibration onto this compressive force significantly impairs cell proliferation and motility, while it does not significantly enhance the loss of viability compared to a static pressure alone (one-way ANOVA, $p = 0.35$). The impact on cell morphology is also more persistent when the particles are set in vibration (Fig. 8). Although we could not clearly attribute the impact of vibrations to a disorganisation of the actin cytoskeleton, we found that particle vibrations indeed alter cellular traction forces, an indirect readout of cytoskeleton integrity (Fig. 10). We observed that this alteration is frequency dependent, being maximal at 2 Hz and 10 Hz while it is lost at 20 Hz. This observation is consistent with our theoretical analysis predicting a cut-off frequency above which the vibration of the MD is dampened.[40] In this previous study, modelling the motion of a MD under an oscillating magnetic field revealed that particle dynamics are governed by the competition between two effects: the tendency of the magnetisation to realign with the applied field (which requires an energetically costly reorientation away from the particle plane and thereby drives particle motion) and the viscoelastic resistence of the intracellular environment, which opposes and delays particle rotation. An increase in frequency was predicted to decrease the amplitude of the MD vibration. A cut-off frequency was estimated in the range [13 Hz–450 kHz] for physiologically relevant values of Young's modulus and viscosity, respectively, in the ranges of [0.05–10] kPa and [10–1000] Pa.s. Our result here suggests that the particle motion is impeded by a viscoelastic medium with a low Young's modulus (on the order of a few tens of Pa) and large viscosity (on the order of several hundreds of Pa.s).

At low frequency, the alteration of contractility levels and the concentration of force points around focal points (Fig. 10) may reflect the laceration of actin filaments. Similar findings were reported by Kumar *et al.*,[69] who showed that cutting single actin filaments using a laser ablation technique leads to a transient increase in cell contractility and localisation of force points around focal adhesions. Indeed, we expect the MD vibration to apply torques in the nN.μm range (Fig. 4). As the excursion angle of the oscillating magnetic field is close to $\theta_0 \simeq 1$ rad, the oscillatory motion of the MD explores a fraction of the arc $R\theta_0 \simeq 0.6$ μm, depending on the visco-elastic properties of the intracellular compartment.[40] Therefore, the force exerted by one vibrating MD on the actin network is likely larger than a few nN, resulting in a local pressure in the order of a few kPa. This value is well above experimental results measuring *in vitro* actin network breakage for stresses of 0.1 Pa.[45] Thus, MD vibration is capable of disrupting the actin cytoskeleton, unlike the vimentin network, which resists much larger strain and stress before breaking.[45] Indeed, we consistently could not observe any depletion of vimentin in the vicinity of vibrating MDs, unlike actin (Fig. S7).

An alternative possibility is that the vibration of particles may be transmitted to the cytoplasmic membrane and activate ion channels. When in contact with the membrane, previous studies showed that particle vibration indeed induces excessive calcium influxes through membrane alteration, triggering cell death.[13] In our experiment, most of the particles are embedded into the cell body, not interacting directly with the cell membrane. Nevertheless, the mechanical strains they generate can propagate to the cytoplasmic membrane. These attenuated perturbations could then trigger the activation of Piezo channels, overexpressed in glioblastoma cells,[70] resulting in calcium influx.[71] Such calcium influxes have been shown to enhance cell contractility and proliferation in glioblastoma-like cells.[72] Furthermore, Piezo channel activation was shown to be sensitive to both the amplitude and the frequency of the mechanical stimulation. For instance, Piezo1 activation in HEK293T cells peaked at 10 Hz when exposed to 5 Pa ultrasonic shear stress, beyond which activation plateaued.[73] This frequency dependence mirrors our observations regarding traction forces (Fig. 10), though not cell growth rates (Fig. 7). In our experimental system, this effect may compete with pro-apoptotic pathways arising from either disruption of the cytoplasmic membrane, as reported by Kim *et al.*[13] or the rupture of internal vesicles. Many MDs are indeed concentrated into autophagosome-like vesicles (Fig. 9), whose membrane rupture could release cytotoxic acidic content. While all these scenarios are plausible and may act in parallel, the precise mechanotransduction pathways activated under these conditions remain to be elucidated. Identifying the specific molecular mediators involved will be essential to fully understand how externally applied magneto-mechanical forces are transduced into biological responses.

At 2 Hz and to a lesser extend at 10 Hz, the alteration in cell contractility persisted for 5 h post-treatment. Within this frequency range, we observed persistent alteration in cell morphology and proliferation 24 h post-treatment (Fig. 7 and 8). These findings support the idea that the alteration of these cellular functions is a consequence of alteration of cell contractility, consistent with numerous studies correlating cell contractility levels with proliferation or migration capabilities.[74–76] However, this correlation did not hold when comparing contractility and cell morphology evolution in cells exposed to a 20 Hz orbital field (Fig. 8d). While the vibration of the MDs had no noticeable effect on cell contractile capabilities, the cell shape was significantly altered, evolving in time toward more rounded shapes. These cells also exhibited the highest death rate (Fig. 7b). While the limited impact on cell contractility can be understood by the reduced deformation of the intracellular material at this larger vibration frequency,[40] it nevertheless results in more severe cellular damage. This suggests that the loss of viability at higher frequency is likely due to the way the particles disorganise the actin (or vimentin) cytoskeleton and other cellular compartments, rather than the amplitude of the perturbing oscillation and stress. These findings also suggest that the cellular response to magneto-mechanical stimulation likely extends beyond the sole activation of mechanosensitive ion channels frequently emphasised in the literature.[13,18] The complexity of the applied mechanical perturbation, combining compression and dynamic actuation, points toward a broader involvement of cytoskeletal and force transmission pathways, which have been shown to play a central role in mechanotransduction and cellular functions. The present study therefore provides the first evidence to interrogate these effects and raises new questions regarding the molecular cascades underlying the observed responses. Addressing these mechanisms will require dedicated investigations integrating molecular and genetic approaches and represents a natural continuation of this work.

5 Conclusions

Overall, our study demonstrates that the mechanical properties of the extracellular environment significantly influence the efficacy of magneto-mechanical stimulation by micrometric magnetic discs. Glioblastoma cells grown on soft polyacrylamide substrates mimicking the stiffness of fibrotic tissues were more sensitive to treatment than those grown on stiff substrates at equal particle loads. This enhanced sensitivity was attributed to stiffness-induced cytoskeletal reorganisation and the resulting changes in cellular rheology. Furthermore, we showed that superimposing vibration onto compressive forces enhances treatment efficacy in a frequency-dependent manner. At low frequencies (2–10 Hz), the mechanical stimulation markedly affected the actomyosin machinery, indicating that the cytoskeleton is a primary target. At higher frequencies (>10 Hz), alterations in morphology, proliferation, and motility did not correlate with actin contractility impairment, suggesting the involvement of additional mechanisms. These findings underscore the potential of magneto-mechanical stimulation as both a standalone and an adjunct nanomedicine strategy for glioblastoma treatment.

Author contributions

AV performed the experiments under the supervision of RM and AN. AV and SS implemented pipelines to analyse the data. RM performed the FEM modelling and simulations. AV, RM and AN analysed and curated the data. AV, RM, BD and AN designed the experiments. BD, RM and AN acquired the project funding, conceptualised the study and developed the methodology. AV, RM and AN wrote the initial draft, which was reviewed and edited by all authors.

Conflicts of interest

AN is a co-founder, shareholder and scientific advisor of Cell&Soft company that provided the pre-coated glass and soft plates for cell culture.

Data availability

The data supporting this article have been included as part of the supplementary information (SI). Supplementary information is available. See DOI: https://doi.org/10.1039/d5na00976f.

Acknowledgements

This work is supported by the French National Research Agency in the framework of the “Investissements d'avenir” program

(ANR-15-IDEX-02). This project received help from the MuLife imaging facility, which is funded by GRAL, a program from the Chemistry Biology Health Graduate School of University Grenoble Alpes (ANR-17-EURE-0003). The authors acknowledge support from the French Renatech network.

Notes and references

1 S. Phuyal, P. Romani, S. Dupont and H. Farhan, *Trends Cell Biol.*, 2023, **33**, 1049–1061.

2 E. Su, C. Villard and J. Manneville, *Biol. Cell*, 2023, **115**, e2300010.

3 K. Molnar and J.-B. Manneville, *npj Biol. Phys. Mech.*, 2025, **2**, 12.

4 A. J. Lomakin, C. J. Cattin, D. Cuvelier, Z. Alraies, M. Molina, G. P. F. Nader, N. Srivastava, P. J. Sáez, J. M. Garcia-Arcos, I. Y. Zhitnyak, A. Bhargava, M. K. Driscoll, E. S. Welf, R. Fiolka, R. J. Petrie, N. S. De Silva, J. M. González-Granado, N. Manel, A. M. Lennon-Duménil, D. J. Müller and M. Piel, *Science*, 2020, **370**, eaba2894.

5 P. Niethammer, *Annu. Rev. Cell Dev. Biol.*, 2021, **37**, 233–256.

6 X. Sun, Z. Zhou, C. Man, A. Leung and A. Ngan, *J. Mech. Behav. Biomed. Mater.*, 2017, **66**, 58–67.

7 X. Wang, C. Ho, Y. Tsatskis, J. Law, Z. Zhang, M. Zhu, C. Dai, F. Wang, M. Tan, S. Hopyan, H. McNeill and Y. Sun, *Sci. Robot.*, 2019, **4**, eaav6180.

8 T. N. Zamay, V. S. Prokopenko, S. S. Zamay, K. A. Lukyanenko, O. S. Kolovskaya, V. A. Orlov, G. S. Zamay, R. G. Galeev, A. A. Narodov and A. S. Kichkailo, *Nanomaterials*, 2021, **11**, 1459.

9 V. Raffa, F. Falcone, S. De Vincentiis, A. Falconieri, M. P. Calatayud, G. F. Goya and A. Cuschieri, *Biophys. J.*, 2018, **115**, 2026–2033.

10 A. Gomez, N. Muzzio, A. Dudek, A. Santi, C. Redondo, R. Zurbano, R. Morales and G. Romero, *Cell. Mol. Bioeng.*, 2023, **16**, 283–298.

11 S. Ponomareva, H. Joisten, T. François, C. Naud, R. Morel, Y. Hou, T. Myers, I. Joumard, B. Dieny and M. Carriere, *Nanoscale*, 2022, **14**, 13274–13283.

12 D. Gregurec, A. W. Senko, A. Chuvilin, P. D. Reddy, A. Sankararaman, D. Rosenfeld, P.-H. Chiang, F. Garcia, I. Tafel, G. Varnavides, E. Ciocan and P. Anikeeva, *ACS Nano*, 2020, **14**, 8036–8045.

13 D.-H. Kim, E. A. Rozhkova, I. V. Ulasov, S. D. Bader, T. Rajh, M. S. Lesniak and V. Novosad, *Nat. Mater.*, 2010, **9**, 165–171.

14 S. Leulmi, H. Joisten, T. Dietsch, C. Iss, M. Morcrette, S. Auffret, P. Sabon and B. Dieny, *Appl. Phys. Lett.*, 2013, **103**, 132412.

15 Y. Cheng, M. E. Muroski, D. C. Petit, R. Mansell, T. Vemulkar, R. A. Morshed, Y. Han, I. V. Balyasnikova, C. M. Horbinski, X. Huang, L. Zhang, R. P. Cowburn and M. S. Lesniak, *J. Controlled Release*, 2016, **223**, 75–84.

16 M. E. Muroski, R. A. Morshed, Y. Cheng, T. Vemulkar, R. Mansell, Y. Han, L. Zhang, K. S. Aboody, R. P. Cowburn and M. S. Lesniak, *PLoS One*, 2016, **11**, e0145129.

17 R. Mansell, T. Vemulkar, D. C. Petit, Y. Cheng, J. Murphy, M. S. Lesniak and R. P. Cowburn, *Sci. Rep.*, 2017, **7**, 1–7.

18 S. Lopez, N. Hallali, Y. Lalatonne, A. Hillion, J. C. Antunes, N. Serhan, P. Clerc, D. Fourmy, L. Motte, J. Carrey and V. Gigoux, *Nanoscale Adv.*, 2022, **4**, 421–436.

19 B. Dieny, A. Visona, C. Naud, H. Joisten, R. Morel, A. Nicolas, M. Carriere, F. Berger and I. J. Mag, *Part. Imag.*, 2024, **10**, 787.

20 C. Boccellato and M. Rehm, *Cell. Oncol.*, 2022, **45**, 527–541.

21 A. Mahdi, M. Aittaleb and F. Tissir, *Cells*, 2025, **14**, 675.

22 L. He, D. Azizad, K. Bhat, A. Ioannidis, C. J. Hoffmann, E. Arambula, M. Eghbali, A. Bhaduri, H. I. Kornblum and F. Pajonk, *Proc. Natl. Acad. Sci. U. S. A.*, 2025, **122**, e2415557122.

23 S. Leulmi Pichot, S. Bentouati, S. S. Ahmad, M. Sotiropoulos, R. Jena and R. Cowburn, *RSC Adv.*, 2020, **10**, 8161–8171.

24 M. Goiriena-Goikoetxea, D. Muñoz, I. Orue, M. L. Fernández-Gubieda, J. Bokor, A. Muela and A. García-Arribas, *Appl. Phys. Rev.*, 2020, **7**, 011306.

25 C. Naud, C. Thébault, M. Carrière, Y. Hou, R. Morel, F. Berger, B. Diény and H. Joisten, *Nanoscale Adv.*, 2020, **2**, 3632–3655.

26 B. Dieny, R. Morel, H. Joisten, C. Naud, A. Nicolas, A. Visonà, P. Obeïd, S. Belin and F. Berger, *Phys. Rev. Appl.*, 2025, **23**, 010501.

27 B. Rashid, M. Destrade and M. D. Gilchrist, *J. Mech. Behav. Biomed. Mater.*, 2012, **10**, 23–38.

28 G. Ciasca, T. E. Sassun, E. Minelli, M. Antonelli, M. Papi, A. Santoro, F. Giangaspero, R. Delfini and M. De Spirito, *Nanoscale*, 2016, **8**, 19629–19643.

29 K.-J. Streitberger, L. Lilaj, F. Schrank, J. Braun, K.-T. Hoffmann, M. Reiss-Zimmermann, J. A. Käs and I. Sack, *Proc. Natl. Acad. Sci. U. S. A.*, 2019, **117**, 128–134.

30 A. Grossen, K. Smith, N. Coulibaly, B. Arbuckle, A. Evans, S. Wilhelm, K. Jones, I. Dunn, R. Towner, D. Wu, Y.-T. Kim and J. Battiste, *Int. J. Mol. Sci.*, 2022, **23**, 4055.

31 A. G. Bhargav, J. S. Domino, R. Chamoun and S. M. Thomas, *Front. Oncol.*, 2022, **11**, 805628.

32 A. Visonà, S. Cavalaglio, S. Labau, S. Soulan, H. Joisten, F. Berger, B. Dieny, R. Morel and A. Nicolas, *Nanoscale Adv.*, 2025, **7**, 219–230.

33 S. R. Peyton and A. J. Putnam, *J. Cell. Physiol.*, 2005, **204**, 198–209.

34 R. K. Assoian and E. A. Klein, *Trends Cell Biol.*, 2008, **18**, 347–352.

35 U. Ben-David, B. Siranosian, G. Ha, H. Tang, Y. Oren, K. Hinohara, C. A. Strathdee, J. Dempster, N. J. Lyons, R. Burns, A. Nag, G. Kugener, B. Cimini, P. Tsvetkov, Y. E. Maruvka, R. O'Rourke, A. Garrity, A. A. Tubelli, P. Bandopadhayay, A. Tsherniak, F. Vazquez, B. Wong, C. Birger, M. Ghandi, A. R. Thorner, J. A. Bittker, M. Meyerson, G. Getz, R. Beroukhim and T. R. Golub, *Nature*, 2018, **560**, 325–330.

36 P.-A. Laval, M. Piecyk, P. Le Guen, M.-D. Ilie, J. Fauvre, I. Coste, T. Renno, N. Aznar, C. Hadji, C. Migdal, C. Duret, P. Bertolino, C. Ferraro-Peyret, A. Nicolas and C. Chaveroux, *Acta Biomater.*, 2024, **182**, 93–110.

37 M. Rovere, D. Reverberi, P. Arnaldi, M. E. F. Palamà and C. Gentili, *Front. Bioeng. Biotechnol.*, 2023, **11**, 1297644.

38 H. Joisten, T. Courcier, P. Balint, P. Sabon, J. Faure-Vincent, S. Auffret and B. Dieny, *Appl. Phys. Lett.*, 2010, **97**, 253112.

39 K. Halbach, *Nucl. Instrum. Methods*, 1980, **169**, 1–10.

40 A. Visonà, R. Morel, H. Joisten, B. Dieny and A. Nicolas, *Nanoscale Adv.*, 2026, **8**, 1570–1584.

41 C. Stringer, T. Wang, M. Michaelos and M. Pachitariu, *Nat. Methods*, 2020, **18**, 100–106.

42 J.-Y. Tinevez, N. Perry, J. Schindelin, G. M. Hoopes, G. D. Reynolds, E. Laplantine, S. Y. Bednarek, S. L. Shorte and K. W. Eliceiri, *Methods*, 2017, **115**, 80–90.

43 A. Mgharbel, C. Migdal, N. Bouchonville, P. Dupenloup, D. Fuard, E. Lopez-Soler, C. Tomba, M. Courçon, D. Gulino-Debrac, H. Delanoë-Ayari and A. Nicolas, *Nanomaterials*, 2022, **12**, 648.

44 J. P. Butler, I. M. Tolic-Nørrelykke, B. Fabry and J. J. Fredberg, *Am. J. Physiol. Cell Physiol.*, 2002, **282**, C595–C605.

45 P. A. Janmey, U. Euteneuer, P. Traub and M. Schliwa, *J. Cell Biol.*, 1991, **113**, 155–160.

46 D. Gonzalez-Rodriguez, L. Guillou, F. Cornat, J. Lafaurie-Janvore, A. Babataheri, E. de Langre, A. I. Barakat and J. Husson, *Biophys. J.*, 2016, **111**, 2711–2721.

47 S. Hughes, S. McBain, J. Dobson and A. J. El Haj, *J. R. Soc., Interface*, 2008, **5**, 855–863.

48 J. Dobson, *Nat. Nanotechnol.*, 2008, **3**, 139–143.

49 A. Prasad and E. Alizadeh, *Trends Biotechnol.*, 2019, **37**, 347–357.

50 M. Théry, A. Pépin, E. Dressaire, Y. Chen and M. Bornens, *Cell Motil. Cytoskelet.*, 2006, **63**, 341–355.

51 P. W. Oakes, S. Banerjee, M. C. Marchetti and M. L. Gardel, *Biophys. J.*, 2014, **107**, 825–833.

52 S. Zhang, H. Gao and G. Bao, *ACS Nano*, 2015, **9**, 8655–8671.

53 J. Debnath, N. Gammoh and K. M. Ryan, *Nat. Rev. Mol. Cell Biol.*, 2023, **24**, 560–575.

54 H. Delanoë-Ayari, N. Bouchonville, M. Courçon and A. Nicolas, *Phys. Rev. Lett.*, 2022, **129**, 098101.

55 S. Leulmi, X. Chauchet, M. Morcrette, G. Ortiz, H. Joisten, P. Sabon, T. Livache, Y. Hou, M. Carrière, S. Lequien and B. Dieny, *Nanoscale*, 2015, **7**, 15904–15914.

56 C. Thébault, M. Marmiesse, C. Naud, K. Pernet-Gallay, E. Billiet, H. Joisten, B. Dieny, M. Carrière, Y. Hou and R. Morel, *Nanoscale Adv.*, 2021, **3**, 6213–6222.

57 T. Jiang, C. Ma and H. Chen, *FASEB Bioadv.*, 2024, **6**, 189–199.

58 J. Solon, I. Levental, K. Sengupta, P. C. Georges and P. A. Janmey, *Biophys. J.*, 2007, **93**, 4453–4461.

59 S.-Y. Tee, J. Fu, C. S. Chen and P. A. Janmey, *Biophys. J.*, 2011, **100**, L25–L27.

60 Y. Abidine, A. Constantinescu, V. M. Laurent, V. S. Rajan, R. Michel, V. Laplaud, A. Duperray and C. Verdier, *Biophys. J.*, 2018, **114**, 1165–1175.

61 D. E. Discher, P. Janmey and Y.-L. Wang, *Science*, 2005, **310**, 1139–1143.

62 M. Gupta, B. R. Sarangi, J. Deschamps, Y. Nematbakhsh, A. Callan-Jones, F. Margadant, R.-M. Mège, C. T. Lim, R. Voituriez and B. Ladoux, *Nat. Commun.*, 2015, **6**, 7525.

63 F. Alisafaei, K. Mandal, R. Saldanha, M. Swoger, H. Yang, X. Shi, M. Guo, H. Hehnly, C. A. Castañeda, P. A. Janmey, A. E. Patteson and V. B. Shenoy, *Commun. Biol.*, 2024, **7**, 658.

64 B. L. Doss, M. Pan, M. Gupta, G. Grenci, R.-M. Mège, C. T. Lim, M. P. Sheetz, R. Voituriez and B. Ladoux, *Proc. Natl. Acad. Sci. U. S. A*, 2020, **117**, 12817–12825.

65 A. N. Ketene, P. C. Roberts, A. A. Shea, E. M. Schmelz and M. Agah, *Integr. Biol.*, 2012, **4**, 540–549.

66 A. E. Patteson, R. J. Carroll, D. V. Iwamoto and P. A. Janmey, *Phys. Biol.*, 2020, **18**, 011001.

67 F. Nunes Vicente, M. Lelek, J.-Y. Tinevez, Q. D. Tran, G. Pehau-Arnaudet, C. Zimmer, S. Etienne-Manneville, G. Giannone and C. Leduc, *Sci. Adv.*, 2022, **8**, eabm2696.

68 J. Ivaska, H.-M. Pallari, J. Nevo and J. E. Eriksson, *Exp. Cell Res.*, 2007, **313**, 2050–2062.

69 S. Kumar, I. Z. Maxwell, A. Heisterkamp, T. R. Polte, T. P. Lele, M. Salanga, E. Mazur and D. E. Ingber, *Biophys. J.*, 2006, **90**, 3762–3773.

70 X. Chen, S. Wanggou, A. Bodalia, M. Zhu, W. Dong, J. J. Fan, W. C. Yin, H.-K. Min, M. Hu, D. Draghici, W. Dou, F. Li, F. J. Coutinho, H. Whetstone, M. M. Kushida, P. B. Dirks, Y. Song, C.-c. Hui, Y. Sun, L.-Y. Wang, X. Li and X. Huang, *Neuron*, 2018, **100**, 799–815.

71 B. Coste, J. Mathur, M. Schmidt, T. J. Earley, S. Ranade, M. J. Petrus, A. E. Dubin and A. Patapoutian, *Science*, 2010, **330**, 55–60.

72 C. Pardo-Pastor, F. Rubio-Moscardo, M. Vogel-González, S. A. Serra, A. Afthinos, S. Mrkonjic, O. Destaing, J. F. Abenza, J. M. Fernández-Fernández, X. Trepat, C. Albiges-Rizo, K. Konstantopoulos and M. A. Valverde, Proceedings of the National Academy of Sciences, 2018, 115, pp. 1925–1930.

73 D. Liao, M.-Y. Hsiao, G. Xiang and P. Zhong, *Sci. Rep.*, 2021, **11**, 709.

74 M. J. Paszek, N. Zahir, K. R. Johnson, J. N. Lakins, G. I. Rozenberg, A. Gefen, C. A. Reinhart-King, S. S. Margulies, M. Dembo, D. Boettiger, D. A. Hammer and V. M. Weaver, *Cancer Cell*, 2005, **8**, 241–254.

75 D. E. Jaalouk and J. Lammerding, *Nat. Rev. Mol. Cell Biol.*, 2009, **10**, 63–73.

76 J. M. Northcott, I. S. Dean, J. K. Mouw and V. M. Weaver, *Front. Cell Dev. Biol.*, 2018, **6**, 17.